Self-aligning active agents with inertia and active torque

Jeremy Fersula
Gulliver UMR CNRS 7083, ESPCI Paris, PSL Research University, 10 Rue Vauquelin, 75005 Paris, France and Institut des Systèmes Intelligents et de Robotique, Sorbonne Université, CNRS, ISIR, F-75005 Paris, France

Nicolas Bredeche
Institut des Systèmes Intelligents et de Robotique, Sorbonne Université, CNRS, ISIR, F-75005 Paris, France

Olivier Dauchot
Gulliver UMR CNRS 7083, ESPCI Paris, PSL Research University, 10 Rue Vauquelin, 75005 Paris, France

(Received 31 January 2024; accepted 27 June 2024; published 15 July 2024)

We extend the study of the inertial effects on the two-dimensional dynamics of active agents to the case where self-alignment is present. In contrast with the most common models of active particles, we find that self-alignment, which couples the rotational dynamics to the translational one, produces unexpected and nontrivial dynamics, already at the deterministic level. Examining first the motion of a free particle, we contrast the role of inertia depending on the sign of the self-aligning torque. When positive, inertia does not alter the steady-state linear motion of an a-chiral self-propelled particle. On the contrary, for a negative self-aligning torque, inertia leads to the destabilization of the linear motion into a spontaneously broken chiral symmetry orbiting dynamics. Adding an active torque, or bias, to the angular dynamics, the bifurcation becomes imperfect in favor of the chiral orientation selected by the bias. In the case of a positive self-alignment, the interplay of the active torque and inertia leads to the emergence, out of a saddle-node bifurcation, of solutions which coexist with the simply biased linear motion. In the context of a free particle, the rotational inertia leaves unchanged the families of steady-state solutions but sets their stability properties. The situation is radically different when considering the case of a collision with a wall, where a very singular oscillating dynamics takes place which can only be captured if both translational and rotational inertia are present.

DOI: 10.1103/PhysRevE.110.014606

I. INTRODUCTION

Self-propelled agents, the "big atoms" of active matter, consume energy to produce directed motion [1–4]. In many cases, such as bacteria [5–8], cells [9–11], manmade Janus [12–17], or rolling colloids [18,19], the agent size together with the viscosity of the surrounding medium ensure that the dynamics take place at sufficiently low Reynolds number and inertia can be neglected [4].

There are, however, other cases, where this simplification does not hold, as, for instance, with the flight of birds [20,21], the motion of vibrated polar grains [22–25], or that of centimetric robots [26–29]. An important effort has been made to upgrade the model of active Brownian particles (ABPs) by including inertia in both translational and orientational motion [30,31]. Analytical results were obtained for the orientational and translational correlation functions of single-particle dynamics with good agreement with experimental results from vibrated granular systems. More exact analytical predictions for higher-order statistics were also obtained in devising an inertial active Ornstein-Uhlenbeck particle, which further simplifies the ABP dynamics by enforcing Gaussian fluctuations [32]. More specifically, it was shown that rotational inertia is fundamentally relevant to reproduce the temporal delay between the active force and particle velocity observed for a single active granular particle.

Another important ingredient to describe polar agents, especially those which take their momentum from a substrate, is self-alignment [33]. Self-alignment was introduced as early as 1996 in the pioneering work of Ref. [34], stemming from the very basic observation that the heading and velocity of a polar body do not need to be parallel. When they are not, the distribution of propulsive and dissipative forces is generically not symmetric concerning the body axis and therefore exerts a torque on the agent body, promoting the reorientation of the latter towards or opposite to its direction of motion. Self-alignment was reintroduced independently in Ref. [9] to describe the collective migration of tissue cells, in Ref. [35] to study active jamming, in Ref. [27] to describe an assembly of wheeled robots, and in Refs. [23,24,36], where it was shown to be a key ingredient for the emergence of collective motion in a system of self-propelled polar disks. More recently, it has started to attract more attention in the context of dense and solid active matter. It was introduced in vertex models [37–40], in phase field models [11], and in a model experimental system of active elastic networks where its central role was elucidated [41,42]. Finally, self-alignment was recently used as a morphological asset in the context of swarm robotics [29].

In light of this growing interest for self-aligning active agents, it is of increasing importance to compute the type of dynamics that arise when self-alignment takes place in

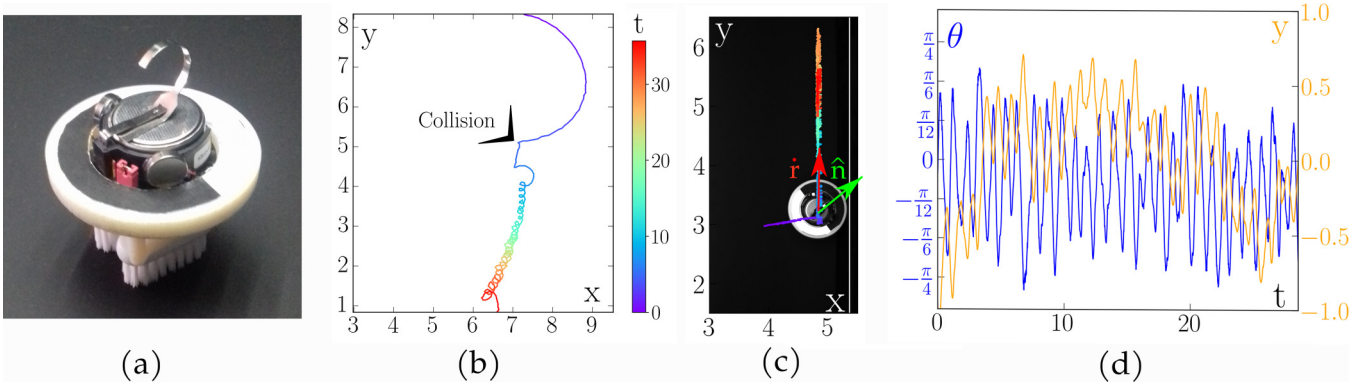

FIG. 1. A few instances of unexpected dynamics observed with an inertial self-aligning agent. (a) A vibebot, combining a standard Kilobot platform [28] with a custom-designed exoskeleton, featuring toothbrush legs in place of the original three metallic rod legs. (b) Such a robot, moving at 10 cm/s, is kicked by an external perturbation while performing a rather large gyration radius circular trajectory, and switches to a rapidly spinning dynamics (see also Supplemental Material Movie 1 [43]). When such augmented Kilobot collisions with a wall with small enough velocity (c) oscillates near its impact point, reorienting periodically (d) (see also Supplemental Material Movie 2), eventually, when the incoming velocity is large and the oscillation amplitude is large enough, the robot escapes the wall (see also Supplemental Material Movie 3).

the presence of inertia, both for a-chiral and chiral agents. Our initial motivation arises from the observations of unexpected dynamics, which we observed while designing low-cost robots. These dynamics are reported on Fig. 1. Following a collision or a manual perturbation, a single freely moving robot can abruptly switch from a circularlike motion to a spinning one, revealing an unexpected coexistence of two very different dynamics for the same value of the control parameters. Collisions with a linear wall revealed even more curious behavior, with the robot facing the wall, while performing a curious angular and translational oscillating motion, around its point of impact. The amplitude of the oscillations increase with the incoming speed, eventually reorienting the robot away from the wall. Such qualitatively intriguing dynamics are absent when the angular dynamics decouples from the translational motion. Our goal is to decipher the respective role of active torque and inertia in setting up these dynamics for self-aligning polar agents. Because the significance of the present paper lies in the generic presence of self-alignment for self-propelled particles taking their momentum from a substrate, we shall also explicitly elucidate the connection of the model equations with the mechanism of motion of an active agent. This analysis further provides a design route to select the sign of the self-aligning torque, as reported in Ref. [29].

The paper is organized as follows. Having shown how self-alignment arises from the distribution of masses and forces on the agent body, we first discuss the case of a free particle before considering the interaction with a linear wall. In the first part, we show that the role of translational inertia depends on the sign of the self-aligning torque. When positive, inertia does not modify the steady-state linear motion of an a-chiral self-propelled particle. However, its interplay with an additional angular bias leads to the emergence, out of a saddle-node bifurcation, of truly unqiue solutions, which coexist with the simply biased linear motion. On the contrary, for a negative self-aligning torque, inertia leads to the destabilization of the linear motion into a spontaneously broken chiral symmetry orbiting dynamics. An additional bias simply turns the bifurcation into an imperfect one in favor of the chiral orientation selected by the bias. As long as a free particle is considered, the rotational inertia leaves unchanged the families of steady-state solutions, except for their linear stability. In the second part, we show that the situation is radically different when considering the case of a collision with a wall. This very singular oscillating dynamics described above can only be captured if both translational and rotational inertia are present.

The active agent considered in this paper is a vibebot, a minimal robot equipped with a small engine that makes it vibrate vertically. Each time, the robot hits the ground, the shape and location of its legs, together with the distribution of mass, transfer a part of the vertical momentum provided by the vibration into horizontal momentum. This propulsion mechanism is common to most artificial walkers used in the field of active matter, from vibrated polar discs [23] to centimetric vibebots [26–29]. Let us first provide an initial intuition of the mechanical origin of self-alignment, following simple symmetry considerations. The first element of design of a self-propelled polar agent is a unit vector $\hat{\boldsymbol{n}}$ describing the tail-head axis of the agent, also called a polar axis, along which it gains momentum due to self-propulsion. For an unbiased agent, the design needs to respect the mirror symmetry of the body with respect to the polar axis, including the distribution of mass, but also the spatial distribution of propulsive and dissipative forces. It is then clear that the very same distribution of mass, propulsive, and dissipative forces are not axially symmetric with respect to the direction of motion, as soon as it is misaligned with the polar axis. This asymmetric distribution of forces exerts a torque on the agent body, which thus rotates its polar axis towards the direction of motion or its opposite.

More formally, the two-dimensional Newton's equations describing the deterministic motion of a self-aligning polar agent heading along $\hat{\boldsymbol{n}} = (\cos\theta, \sin\theta)$ in the direction θ read

$$m\ddot{\boldsymbol{r}} = F_a\hat{\boldsymbol{n}} + \tilde{\boldsymbol{F}}_{\text{ext}}(\boldsymbol{r}) - \gamma\dot{\boldsymbol{r}}, \tag{1a}$$

$$\tilde{J}\ddot{\theta} = \tilde{T}_a + \zeta(\hat{\boldsymbol{n}} \times \dot{\boldsymbol{r}}) \cdot \boldsymbol{e}_z - \gamma_r\dot{\theta}. \tag{1b}$$

where m r and $\tilde{J}$, respectively, are the mass, position, and inertial momentum of the agent, and γ, γ_r, respectively, encode the translational and rotational damping, which are assumed to be scalar. The first equation describes the inertial translational motion of an active agent self-propelled by an active force $F_a\hat{\boldsymbol{n}}$, subject to an external force $\tilde{\boldsymbol{F}}_{\rm ext}(\boldsymbol{r})$ and experiencing a drag force $-\gamma\dot{\boldsymbol{r}}$. The second equation expresses the inertial reorientation of the active force, subject to an active torque $\tilde{T}_a$, self-alignment, and angular damping. The active torque arises from a possible chirality of the active particle, also called bias if undesired. The self-aligning term expresses the coupling between the velocity of the particle and the orientation of the active force when they are not colinear. When ζ is positive, respectively, negative, the coupling tends to align, respectively, antialign, $\hat{\boldsymbol{n}}$ with $\dot{\boldsymbol{r}}$. More precisely, the active torque and the self-aligning term arise from the distribution of the contacts of the agent with the ground. Consider a two-dimensional rigid body, with N contacts located at positions $\boldsymbol{r}_i$. These contacts are the points of application of the propelling forces $\boldsymbol{f}_i^a$ and dissipative forces $-\gamma_i\dot{\boldsymbol{r}}_i$, where γ_i, the damping coefficient, may vary from one contact to another. The kinematics of a rigid body imposes that

$$\dot{\boldsymbol{r}}_i = \dot{\boldsymbol{r}}_{\rm cm} + \boldsymbol{\Omega}\times(\boldsymbol{r}_i - \boldsymbol{r}_{\rm cm}), \tag{2}$$

with $\boldsymbol{r}_{\rm cm}$ the center of mass and $\boldsymbol{\Omega} = \dot{\theta}\boldsymbol{e}_z$ the solid body rotation. The total momentum arising from the contact with the ground,

$$\boldsymbol{T} = \sum_i (\boldsymbol{r}_i - \boldsymbol{r}_{\rm cm})\times\left(\boldsymbol{f}_i^a - \gamma_i\dot{\boldsymbol{r}}_i\right), \tag{3}$$

thus reads

$$\boldsymbol{T} = \tilde{\boldsymbol{T}}_a - \gamma(\boldsymbol{r}_{cf} - \boldsymbol{r}_{\rm cm})\times\dot{\boldsymbol{r}}_{\rm cm} - \gamma_r\dot{\theta}\boldsymbol{e}_z, \tag{4}$$

where $\tilde{\boldsymbol{T}}_a = \sum_i(\boldsymbol{r}_i - \boldsymbol{r}_{\rm cm})\times\boldsymbol{f}_i^a$ is the active torque, $\gamma = \sum_i\gamma_i$ is the total damping coefficient, $\boldsymbol{r}_{cf} = \sum_i\gamma_i\boldsymbol{r}_i/\gamma$ is the center of friction, and $\gamma_r = \sum_i\gamma_i|\boldsymbol{r}_i - \boldsymbol{r}_{\rm cm}|^2$ is the rotational damping. For a mirror symmetric body with respect to the polar axis, $\boldsymbol{r}_{cf} - \boldsymbol{r}_{\rm cm}$ and $\hat{\boldsymbol{n}}$ are colinear, so the law of momentum reads as Eq. (1b), with $\zeta = \gamma(\boldsymbol{r}_{\rm cm} - \boldsymbol{r}_{cf})\cdot\hat{\boldsymbol{n}}$. One sees that the sign of ζ is directly set by the position of the center of friction relatively to the center of mass, along the polar axis.

Equations (1) were shown to faithfully describe the motion of a self-propelled polar agent in a harmonic potential, as experimentally observed with the simple Hexbug robot device running in a parabola dish [44]. The onset of collective motion in a system of self-aligning hard disks was also captured [36,45], as observed experimentally and numerically in a system of vibrated polar grains [23,24,46]. Note that in some other context [9,34,35], the self-aligning torque can be normalized by the norm of $\dot{\boldsymbol{r}}$.

In the following, we shall respectively use m, the body length d of the agent, and d/v_0, with $v_0 = F_a/\gamma$ the free flight velocity, as the mass, length, and time units. The dimensionless equations then read

$$\tau_v\ddot{\boldsymbol{r}} = \hat{\boldsymbol{n}} - \dot{\boldsymbol{r}} + \boldsymbol{F}_{\rm ext}(\boldsymbol{r}), \tag{5a}$$

$$J\ddot{\theta} = T_a + \epsilon(\hat{\boldsymbol{n}}\times\dot{\boldsymbol{r}})\cdot\boldsymbol{e}_z - \tau_n\dot{\theta}, \tag{5b}$$

with $\boldsymbol{F}_{\rm ext} = \frac{\tilde{\boldsymbol{F}}_{\rm ext}}{\gamma v_0}$ and $T_a = \frac{\tilde{T}_a}{|\zeta|v_0}$, $J = \frac{\tilde{J}v_0}{|\zeta|d^2}$, $\tau_v = \frac{mv_0}{\gamma d}$, $\tau_n = \frac{\gamma_r}{|\zeta|d}$ and $\epsilon = \text{sign}(\zeta)$.

II. FREE PARTICLE DYNAMICS

In the absence of external force, the isotropy of space imposes that only the difference of orientation between $\hat{\boldsymbol{n}}$ and $\boldsymbol{v} = \dot{\boldsymbol{r}}$ matters. Introducing the orientations ϕ of $\boldsymbol{v} = v\binom{\cos\phi}{\sin\phi}$ and θ of $\hat{\boldsymbol{n}} = \binom{\cos\theta}{\sin\theta}$, together with their difference $\alpha = \theta - \phi$, one obtains the equations for the free particle dynamics:

$$\tau_v\dot{\phi} = \frac{1}{v}\sin\alpha, \tag{6a}$$

$$\tau_v\dot{v} = \cos\alpha - v, \tag{6b}$$

$$\dot{\alpha} = \omega - \frac{1}{\tau_v v}\sin\alpha, \tag{6c}$$

$$J\dot{\omega} = T_a - \epsilon v\sin\alpha - \tau_n\omega, \tag{6d}$$

where $\omega = \dot{\theta}$. The last three equations form a closed system for the variable (v, α, ω), the solution of which sets the dynamics of ϕ through the first equation.

The steady-state dynamics are obtained by solving for the fixed points of equations (6) and performing their linear stability analysis. Equations (A1b) and (A1c) readily lead to $v^* = \cos\alpha^*$ and $\omega^* = \frac{1}{\tau_v}\tan\alpha^*$. Substituting in Eq. (A1d) and denoting $t = \tan\alpha^*$, one finds the third-order polynomial in t, the roots of which set the fixed points:

$$\frac{\tau_n}{\tau_v}t^3 - T_a t^2 + \left(\epsilon + \frac{\tau_n}{\tau_v}\right)t - T_a = 0. \tag{7}$$

A. Unbiased inertial dynamics, $T_a = 0$

It is instructive to start with the case of an a-chiral, or unbiased, particle, $T_a = 0$, for which obtaining the steady-state solutions and their stability is straightforward. The results are summarized in Fig. 2. One immediately identifies the trivial fixed point $t = 0$, leading to $v^* = 1$, $\alpha^* = 0$, $\omega^* = 0$, $\dot{\phi}^* = 0$, which corresponds to the particle performing straight motion at nominal velocity, with $\boldsymbol{v}$ and $\hat{\boldsymbol{n}}$ being aligned. In the aligning case, $\epsilon = +1$ (blue lines in Fig. 2), this is the only fixed point and it is always linearly stable. In the antialigning case, $\epsilon = -1$ (green lines in Fig. 2), two mirror fixed points, given by $\tan\alpha^* = \pm\sqrt{-(1 + \epsilon\tau_v/\tau_n)}$ emerge from a a pitchfork bifurcation, when the linear motion turns unstable for $\tau_v/\tau_n > 1$. These fixed points describe clockwise and anticlockwise circular trajectories, with an orbiting frequency $\omega^* = \dot{\phi}^* = \frac{1}{\sqrt{\tau_n\tau_v}}\sin\alpha^*$ and a radius $R^* = v^*/\omega^* = \frac{1}{\tau_v\sin\alpha^*}$. Note the nonmonotonic dependence of the rotation frequency with τ_v/τ_n: it arises from the combination of the fast increase of α^* at the onset of the instability and the $1/\sqrt{\tau_v}$ prefactor expressing the slowing down of the dynamics by inertia.

The physical picture is as follows. In both cases, the velocity $\boldsymbol{v}$ tends to align with the orientation $\hat{\boldsymbol{n}}$ imposed by the active force. In the aligning case, $\hat{\boldsymbol{n}}$ rotates toward $\boldsymbol{v}$, so independently of the timescales of the dynamics, the two vectors dynamics stabilize the steady state where they are aligned. Conversely, in the antialigning case, $\hat{\boldsymbol{n}}$ rotates *away* from $\boldsymbol{v}$.

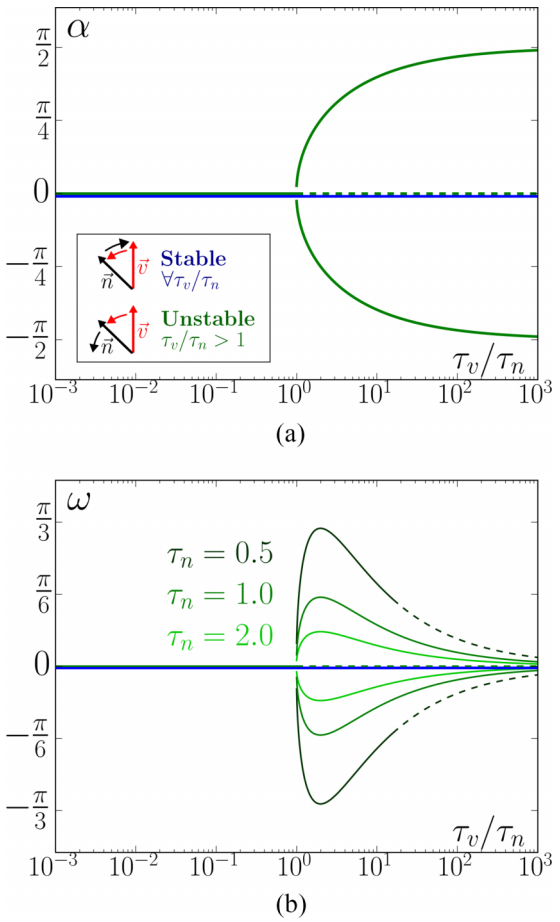

FIG. 2. Bifurcation diagram for the steady-state dynamics of a free self-aligning particle with inertia and no bias: (a) angle between the orientation and the velocity vector. Inset: While the aligning dynamics is stabilizing the dynamics, the antialigning one is destabilizing. (b) Orbiting frequency. In blue, respectively, green: aligning, respectively, antialigning case. Continuous, respectively, dotted lines denote linearly stable, respectively, unstable solutions.

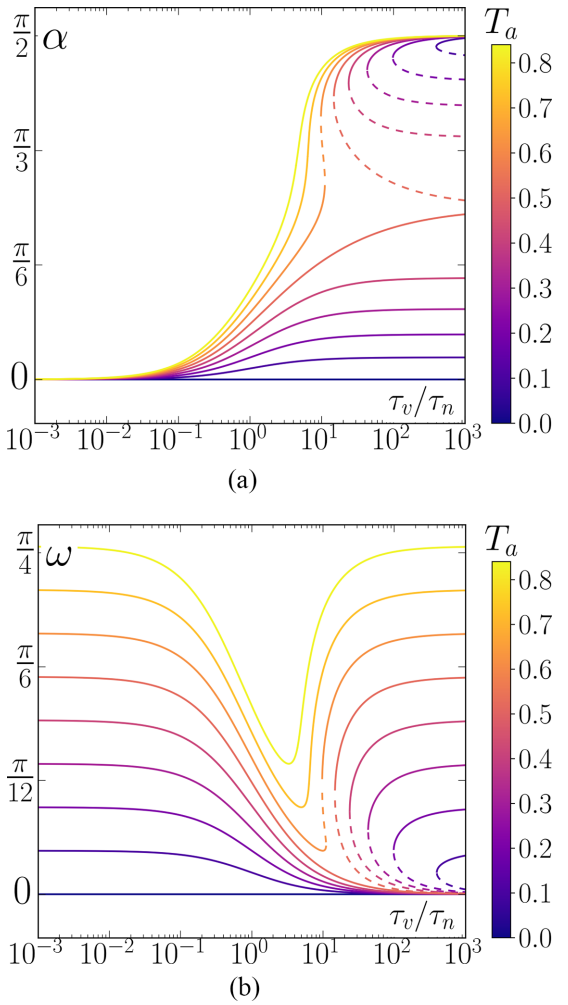

FIG. 3. Free inertial dynamics of aligning chiral particles. (a) Misalignment, α^*, between the velocity and the orientation of the self-propelling force and (b) angular frequency, ω^*, of the resulting circular motions as a function of τ_v/τ_n for increasing values of the bias, as indicated by the color code. Continuous, respectively, dotted lines denote linearly stable, respectively, unstable solutions.

Whenever τ_v/τ_n is too large, $\boldsymbol{v}$ cannot catch up with $\hat{\boldsymbol{n}}$, and any small disturbance of the linear motion destabilizes it in an endless orbiting motion. The angular inertia does not alter the family of solutions, but as we shall discuss below, it conditions the stability properties of these solutions. We conclude this section by recalling that, to our knowledge, there is so far only one experimental realization of an antialigning polar particle, a kilobot augmented with a specific 3D exoskeleton described in Ref. [29]. The orbiting solution pinpointed here was not reported in that work; the reason being that the inertia of such robots is small enough to avoid the destabilization of the straight motion.

B. Inertial dynamics of chiral particles, $T_a \neq 0$

In the presence of an active torque, the analytical solutions provided by solving for the roots of Eq. (A3) have a cumbersome dependence on the parameters. Their domains of existence are provided in the Appendix. However, one can make a few simple statements by considering limiting cases. In the limit of vanishing translational inertia, $\frac{\tau_v}{\tau_n} \to 0$, the only solution is $\alpha^* \to 0$, $v^* \to 1$ and $\omega^* \to T_a/\tau_n$. It corresponds to circular trajectories with a radius $R^* \to \tau_n/T_a$, which diverges in the a-chiral limit: they simply form the generalization of the straight trajectories bended by the bias. Conversely, in the limit of large translational inertia, $\frac{\tau_v}{\tau_n} \to \infty$, the situation becomes qualitatively different. For $|T_a| < 1/2$, three solutions exists, one of which is given by $\alpha^* \to \pm\frac{\pi}{2}$, $v^* \to 0$, and $\omega^* \to T_a/\tau_n$. For $|T_a| > 1/2$, only this solution subsists. It corresponds to a purely spinning dynamics, where the particle rotates on itself. The connection between the two limits is summarized in Figs. 3 and 4 for the aligning and antialigning case, respectively. In the aligning case, $\epsilon = +1$, one finds an unexpectedly rich bifurcation diagram. As expected, the linear motion obtained when $T_a = 0$ is replaced by the slowly rotating circular motion, with $\omega^* = \frac{\tan\alpha^*}{\tau_v}$, the radius of which $R^* = \frac{1}{\tau_v \sin\alpha^*}$ decreases from infinity when the bias grows from zero. This solution is always linearly stable. More surprising are the two solutions which emerge from a saddle-node bifurcation above a bias-dependent critical value

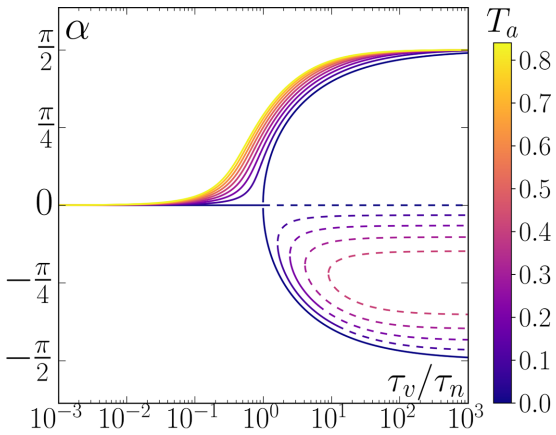

(a)

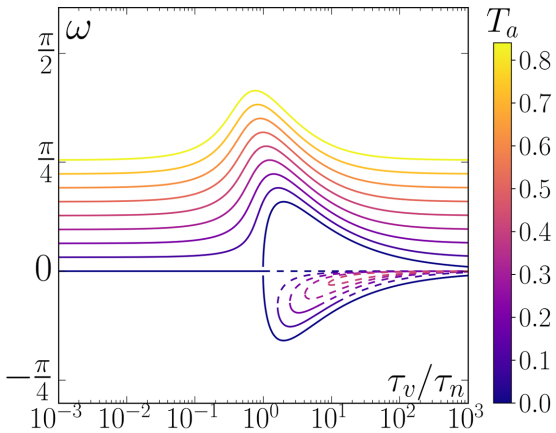

(b)

FIG. 4. Free inertial dynamics of an antialigning chiral particle: (a) Misalignment, α^*, between the velocity and orientation of the self-propelling force and (b) angular frequency, ω^*, of the resulting circular motions as a function of τ_v/τ_n for increasing values of the bias, as indicated by the color code. Continuous, respectively, dotted lines denote linearly stable, respectively, unstable, solutions.

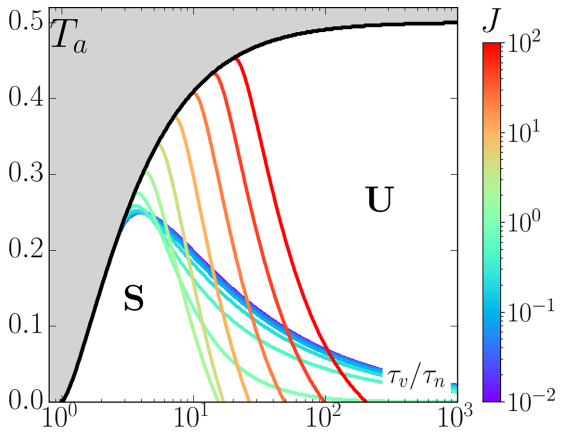

FIG. 5. Domain of existence and stability of the lowest branch of the bifurcated solutions, in the case $\epsilon = -1$: The grey area denotes the region in the $(\tau_v/\tau_n, T_a)$ plane, where the solution does not exist. In the existence domain, the solution is stable to the left of a line, the position of which is set by the angular inertia, as indicated by the color code ($\tau_n = 1$).

of τ_v/τ_n. The fastest one, with a small radius of gyration, converges to the spinning solution described above in the limit of large inertia $\tau_v/\tau_n \to \infty$ and is stable. The slower one is always unstable. Below this bias-dependent critical value of τ_v/τ_n, the lower branch disappears and the faster branch merges with the slowly rotating circular motion inherited from the straight motion, in the absence of bias.

Comparatively, the antialigning case, $\epsilon = -1$, is a straightforward generalization of the bifurcation diagram obtained in the absence of bias. For $T_a < T_a^*(\tau_v/\tau_n)$, the active torque simply renders the pitchfork bifurcation imperfect in a way analogous to the effect of an external field on a paraferromagnetic transition. The bifurcated branch compatible with the bias merges continuously with the slowly rotating circular motion inherited from the straight motion in the absence of bias. The other one connects in a saddle-node bifurcation to the one inherited from the linearly unstable straight trajectory. For $T_a > T_a^*$, only the linearly stable strongly biased solution persists.

We close this section by discussing the nontrivial dependence on the angular inertia of the linear stability of the bifurcated solutions in the antialigning case. The solution inherited from the linearly unstable straight trajectory remains unstable, as it should. On the contrary, the linear stability of the solution inherited from the bifurcated solution opposing the bias depends on the angular inertia J and τ_n. Figure 5 displays the existence and stability domains of these solutions, in the $(\tau_v/\tau_n, T_a)$ plane for $\tau_n = 1$ and different values of J. As stated above, the bias sets the domain of existence of the solutions: the larger T_a, the larger the value of τ_v/τ_n above which these non-trivial solutions exist. A finite angular inertia imposes a bias-dependent maximal value to τ_v/τ_n, above which the solution turns linearly unstable. For small J, the so-obtained domain of stability shrinks when J increases. For J larger than a threshold of the order of τ_n, this tendency reverses: the linear stability enlarges with growing J, eventually recovering stable solutions in all their domains of existence in the limit $J \to +\infty$. A similar dependence is observed for an increase of $1/\tau_n$ at a fixed value of J, highlighting the similar role played by the two quantities. The basis of the linear analysis is provided in the Appendix.

In conclusion, the above results demonstrate the key role of self-alignment, when it combines with translational inertia, in producing qualitatively steady dynamics even in the simplest case of freely moving particles. For the aligning case, the straight-line trajectory remains the only solution in the absence of bias. Any small amount of bias gives rise to a branch of solutions disconnected from the previous one, which corresponds to a rapidly spinning motion. Such a solution coexists with the quasilinear motion. For the antialigning case, two branches of chiral orbiting solutions emerge at large inertia even in the absence of bias. In the absence of external forces, the rotational inertia only affects the stability of these steady dynamics. We shall now see that it becomes a central ingredient when describing the interaction of such a particle with a linear hard wall.

III. COLLISION WITH A WALL

Performing experiments with self-propelled agents, one usually confines them in one way or another, typically using lateral walls. Figures 1(c)–1(e) report the motion of an inertial aligning agent, when it enters into contact with a wall. For low enough incoming velocity, one observes that, after a short transient, the self-aligning agent performs an endless translational and orientational oscillation along the wall. The amplitude of these oscillations increases with the incoming speed. When the amplitude of the angular oscillation is so large that it reorients the agent away from the wall, the latter escapes the wall.

This intriguing dynamics is well captured by Eqs. (5), where the external force now describes the interaction with the wall. As we shall see, the bias is not a necessary ingredient and we omit it from now on, for the purpose of simplicity. Let us denote $\hat{\boldsymbol{e}}_x$ the direction towards the wall and $\hat{\boldsymbol{e}}_y$ the direction parallel to the wall [see Fig. 1(c)] with the wall sitting in the position $x = 0$. In light of the rolling motion observed experimentally, the most general description of this interaction is that of

(1) a repulsive force in the direction normal to the wall: $F_w^{\perp} = -\frac{\partial V_w(\boldsymbol{r})}{\partial x} = -\frac{\epsilon_w}{d} N_w$, with $-N_w$ being the dimensionless force normal to the wall;

(2) a tangential frictional force opposing the sliding velocity u: $F_w^{\parallel} = -\mu u$, with $u = v_y + \frac{d}{2}\dot{\theta}$, where the second term accounts for the rotation of the contact point with the wall; and

(3) a torque resulting from the friction at contact: $\Gamma_w = -\mu \frac{d}{2} u$.

The precise choice of the repulsive potential is not crucial as long as it is stiff enough. In the following, V_w is a Weeks-Chandler-Andersen potential, leading to a normal force

$$N_w = 16n\left(\left(\frac{\sigma}{|x|}\right)^{2n+1} - \frac{1}{2}\left(\frac{\sigma}{|x|}\right)^{n+1}\right),$$

with $\sigma = d/2^{1+1/n}$ and $n = 6$. Finally, the interaction with the wall is truncated and set to zero when the distance to the wall is $|x| > 2^{1/n}\frac{d}{2}$. Altogether, the dimensionless equations describing the dynamics of a self-aligning agent in contact with the wall read:,

$$\tau_v \ddot{x} = \cos\theta - \dot{x} - \kappa N_w(x), \tag{8a}$$

$$\tau_v \ddot{y} = \sin\theta - \dot{y} - \nu(\dot{y} + \dot{\theta}/2), \tag{8b}$$

$$J\ddot{\theta} = \epsilon(\cos\theta\, \dot{y} - \sin\theta\, \dot{x}) - \tau_n \dot{\theta} - \tau_r(\dot{y} + \dot{\theta}/2), \tag{8c}$$

where τ_v, J, τ_n, ϵ are as defined in the previous section and the additional dimensionless parameters are $\kappa = \frac{\epsilon_w}{\gamma v_0 d}$, $\nu = \frac{\mu}{\gamma}$, and $\tau_r = \frac{\mu d}{2\zeta}$.

As a further simplification, we shall assume that the relevant part of the dynamics takes place along the wall, while the dynamics perpendicular to the wall consist of a rapid equilibration of the propelling force and the repulsive one. This is possible because the wall is not infinitely rigid and the position within the wall can accommodate the variation of the propelling force in the direction normal to the wall according to the balance $\cos\theta = \kappa N_w(x)$. Within this assumption, Eqs. (8) reduce to four first-order differential equations for the variables $(y, \dot{y}, \theta, \dot{\theta})$ provided in the Appendix. We shall verify below that this assumption is valid by performing simulations of the above equations, once a better understanding of the mechanisms is at play, which will allow us to select the proper range of values for the numerous control parameters.

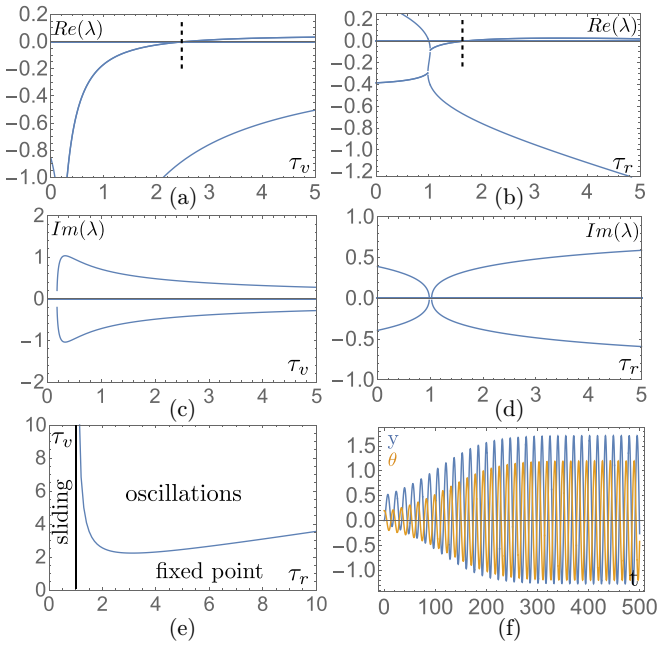

FIG. 6. Linear stability of the fixed point against the wall in the aligning case, $\epsilon = +1$. (a)–(c) Real and imaginary parts of some, including the largest, eigenvalues as a function of τ_v for $\tau_r = 2$. For large enough inertia, the fixed point facing the wall turns unstable via a Hopf bifurcation (vertical dotted line). (b)–(d) Real and imaginary parts of the eigenvalues as a function of τ_r for $\tau_v = 3$: For $\tau_r < 1$, there is always a positive real part and the fixed point is unstable; for $\tau_r > 1$, there is a small range of τ_r values for which the fixed point is stable before it turns unstable via a Hopf bifurcation (vertical dotted line). (e) The critical value of τ_v above which oscillations take place depends in a nonmonotonous way on τ_r. (f) The oscillating dynamics for $\tau_v = 3$ and $\tau_r = 2$. In all panels, $J = \tau_v$, $\tau_n = 0.1$, $\nu = 0.1$.

The dynamics described by Eqs. (8), reduced to the dynamics along y and θ, have two infinite sets of fixed points $(y^* = y_0, \theta^* = 0 \text{ or } \pi, \dot{y}^* = 0, \dot{\theta}^* = 0)$ corresponding to the active agent pointing statically into or outward the wall at any position y_0, the case where the agent points outward being irrelevant here. In the absence of inertia, these fixed points are marginally stable, reflecting the translational invariance along y.

In the aligning case, $\epsilon = +1$, for any small amount of inertia, any of these fixed points becomes linearly unstable for $\tau_r < 1$ [Figs. 6(b) and 6(d)] and the dynamics obey another steady solution given by $(y_s = v_0 t, \theta_s = \arccos(\tau_r), \dot{y}_s = v_0 = \sin\theta_s/(1+\nu), \dot{\theta}_s = 0)$, describing the sliding motion of the active agent along the wall. When $\tau_r > 1$, the linear stability of the fixed point depends on the respective values of all the parameters, but can be summarized as follows. For a given value of the damping coefficients ν and τ_n, there is a critical inertia above which the fixed point turns unstable in favor of periodic dynamics through a Hopf bifurcation [Figs. 6(a) and 6(c)], leaving the place for the oscillations

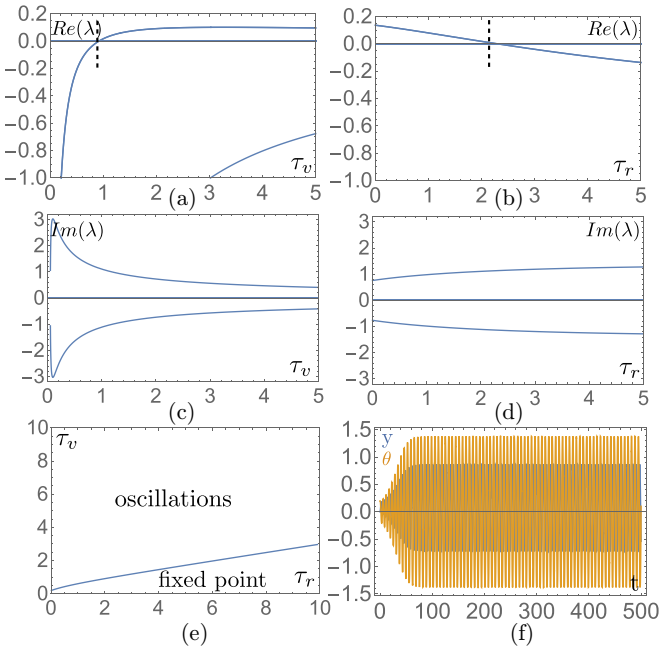

FIG. 7. Linear stability of the fixed point against the wall in the antialigning case, $\epsilon = -1$. (a)–(c) Real and imaginary parts of some, including the largest, eigenvalues as a function of τ_v for $\tau_r = 2$: for large enough inertia, the fixed point facing the wall turns unstable via a Hopf bifurcation (vertical dotted line). (b)–(d) Real and imaginary parts of the eigenvalues as a function of τ_r for $\tau_v = 1$: For large enough friction with the wall, the fixed point facing the wall turns unstable via a Hopf bifurcation (vertical dotted line). (e) The critical value of τ_v above which oscillations take place is a simple increasing function of τ_r. (f) The oscillating dynamics for $\tau_v = 1$ and $\tau_r = 2$. In all panels, $J = \tau_v$, $\tau_n = 0.1$, $\nu = 0.1$.

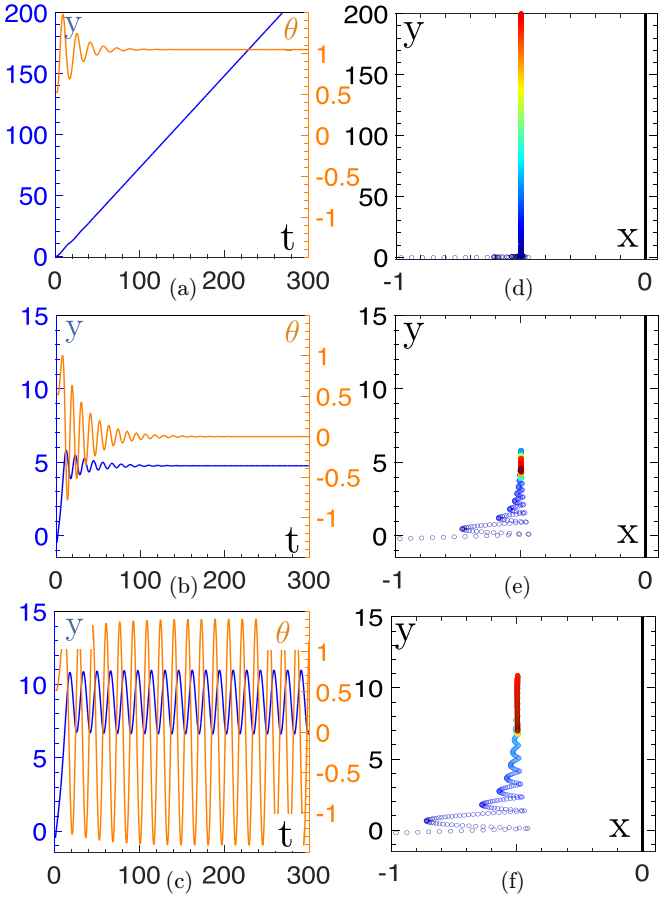

FIG. 8. 2D trajectories against the wall in the aligning case, $\epsilon = +1$: (a)–(c) y, coordinate along the wall, and θ, the orientation of the active agent as a function of time for the sliding dynamics, the static fixed point, and the oscillating dynamics, respectively; (d)–(f) corresponding trajectories in the (x, y) plane. The vertical black line denotes the position of the wall; the trajectories are color coded from blue to red by increasing time; in the initial condition, the agent sits in $(x = -1, y = -0.5)$ and points in the direction $\theta = \pi/6$. The parameter values are for (a), (d): $\tau_v = 0.5$, $J = 4$, $\tau_r = 0.5$, $\nu = 0.15$, $\tau_n = 0.15$; for (b), (e): $\tau_v = 1$, $J = 4$, $\tau_r = 3$, $\nu = 0.15$, $\tau_n = 0.15$; and for (c), (f): $\tau_v = 1.5$, $J = 9$, $\tau_r = 3$, $\nu = 0.15$, $\tau_n = 0.15$.

observed experimentally [Fig. 6(f)]. Both translational and angular inertia must be nonzero for this instability to take place. Increasing the damping coefficients simply increases the value of the critical inertia. For a fixed ratio of angular to translational inertia, the dependence of the critical inertia on τ_r is not necessarily monotonic [Fig. 6(e)].

In the antialigning case, the situation is somehow simpler because the sliding solution does not exist. The relevant fixed points remain marginal in the absence of inertia [Figs. 7(a) and 7(c)], whatever the value of τ_r. For large enough inertia and not too large τ_r, any of the translationally equivalent fixed point turns unstable via a Hopf bifurcation [Figs. 7(b) and 7(d)], leading to the same type of oscillatory dynamics as in the aligning case [Fig. 7(f)]. Here the critical inertia is a simple increasing function of τ_r [Fig. 7(e)]. As in the aligning case, increasing the damping coefficients ν and τ_n simply increases the value of the critical inertia.

Both in the aligning and antialigning cases, one numerically checks that the amplitude of the oscillations increases with inertia until eventually θ reaches values larger than $\pi/2$, the agent leaves the wall, and the present simplified description stops holding.

As stated initially, the above reduction of the dynamics to a simpler one-dimensional motion along the wall assumes a permanent contact with the wall which is different from the repeated collisions experienced by a real hard body active agent, such as the vibebot of Fig. 1(a). Performing simulations of the full set of Eqs. (8), we confirm the validity of the approach, as the same dynamics are observed in the good range of values for the control parameters. In the aligning case, the three dynamics identified previously are reported in Fig. 8. For $\tau_r < 1$ [Figs. 8(a)–8(d)], the agent indefinitely slides along the wall. This behavior was tested experimentally using an alternative vibebot with a smaller τ_r value. Only the sliding dynamics were observed (see Supplemental Material, Movie 4). For $\tau_r > 1$ and small inertia [Figs. 8(b) and 8(e)], damped oscillations follow an initial bouncing regime before the agent sets in a static position facing the wall. For $\tau_r > 1$ and large inertia [Figs. 8(c) and 8(f)], sustained oscillations follow the same initial regime. The two dynamics predicted for the antialigning case are also recovered. Independently of the value of τ_r, for small enough inertia [Fig. 9(a)], the agent rapidly stabilizes into the static fixed point [Fig. 9(a)],

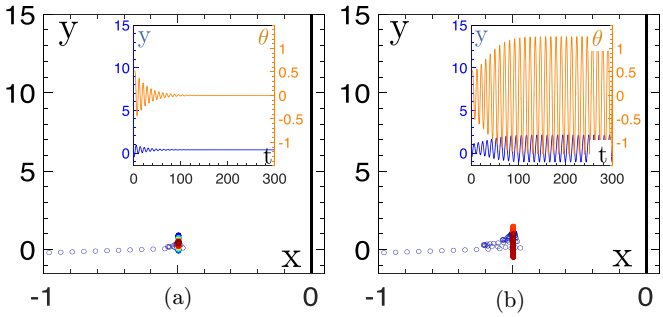

FIG. 9. 2D trajectories against the wall in the antialigning case, $\epsilon = -1$. (a), (b) y, coordinate along the wall, and θ, the orientation of the active agent as a function of time for the static fixed point, and the oscillating dynamics, respectively (insets); corresponding trajectories in the (x, y) plane; the vertical black line denotes the position of the wall; the trajectories are color coded from blue to red by increasing time; in the initial condition, the agent sits in $(x = -1, y = -0.5)$ and points in the direction $\theta = \pi/6$. The parameter values are for (a) $\tau_v = 0.2, J = 3, \tau_r = 1, \nu = 0.15, \tau_n = 0.15$ and (b) $\tau_v = 0.5, J = 3, \tau_r = 1, \nu = 0.15, \tau_n = 0.15$.

while for larger inertia the oscillations set in [Fig. 9(b)]. Note the difference in the transitory regime, which is much more localized around the impact point in the antialigning case than in the aligning one.

IV. CONCLUSION

Coupling inertia with self-alignment considerably enriches the deterministic dynamics of self-propelled active agents. As in the case of standard active particles, translational inertia hinders the agent's ability to change the direction of its velocity in response to the active and external forces and angular inertia does the same for the direction of the self-propulsion in response to torques. Self-alignment, because of the coupling with the translational degrees of freedom, does not simply act like an active torque. In the aligning case, it reduces the inertial delay between the orientation of self-propulsion and the velocity. Conversely, in the antialigning case, it increases this delay.

In light of the relevance of inertial self-alignment for large active agents that take their momentum from a substrate, such as walking robots and animals or rolling vehicles, the dynamics discussed here could contribute to better control of such agents. The role of inertia in the emergence of collective dynamics in a large population of such agents is also a matter of important concern. It was shown that collective motion in a population of self-aligning particles arises from the relaxation dynamics of the polarities of the particles towards their respective velocities, following collisions [36,45]. Our results demonstrate that in the presence of angular inertia, the collision rules are qualitatively different, suggesting here also a major impact on the onset of collective dynamics. Finally, the next step is obviously to consider the role of noise on such dynamics, following the work of Refs. [30,31], a technical challenge, given the coupling of positional and translational degrees of freedom.

ACKNOWLEDGMENTS

This work was supported by the MSR project funded by the Agence Nationale pour la Recherche under Grant No. ANR-18-CE33-0006. J.F. was supported by a Ph.D. grant from SCAI – Sorbonne Center for Artificial Intelligence.

APPENDIX

In this appendix, we provide more detailed calculations for the linear stability analysis, of the steady dynamics reported in the main text. More specifically, we provide the explicit form of the Jacobian for each case.

1. Solutions and stability of the free particle dynamics

We start with Eqs. (6) of the main text:

$$\tau_v \dot{\phi} = \frac{1}{v}\sin\alpha, \tag{A1a}$$

$$\tau_v \dot{v} = \cos\alpha - v, \tag{A1b}$$

$$\dot{\alpha} = \omega - \frac{1}{\tau_v v}\sin\alpha, \tag{A1c}$$

$$J\dot{\omega} = T_a - \epsilon v \sin\alpha - \tau_n \omega, \tag{A1d}$$

where we recall that the last three equations form a closed system for the variable (v, α, ω), the solution of which sets the dynamics of ϕ through the first equation. Solving for the fixed points, Eqs. (A1b) and (A1c) lead to $v^* = \cos\alpha^*$ and $\omega^* = \frac{1}{\tau_v}\tan\alpha^*$. Substituting in Eq. (A1d) and denoting $t = \tan\alpha^*$, one finds the third-order polynomial in t:

$$\frac{\tau_n}{\tau_v}t^3 - T_a t^2 + \left(\epsilon + \frac{\tau_n}{\tau_v}\right)t - T_a = 0. \tag{A2}$$

a. Case $T_a = 0$

The above equation reduces to

$$\frac{\tau_n}{\tau_v}t^3 + \left(\epsilon + \frac{\tau_n}{\tau_v}\right)t = 0, \tag{A3}$$

with solutions $t_0 = 0$, which always exist, and $t_\pm = \pm\sqrt{-(1 + \epsilon\frac{\tau_v}{\tau_n})}$, which only exist if $1 + \epsilon\frac{\tau_v}{\tau_n} \leqslant 0$, that is, for $\epsilon = -1$ (antialignment) and $\frac{\tau_v}{\tau_n} \geqslant 1$.

The linear stability of these solutions is provided by the analysis of the sign of the real part of the eigenvalues of the Jacobian,

$$K_0 = \begin{pmatrix} -\frac{1}{\tau_v} & -\frac{\sin\alpha}{\tau_v} & 0 \\ \frac{\sin\alpha}{\tau_v v^2} & -\frac{\cos\alpha}{\tau_v v} & 1 \\ -\frac{\epsilon\sin\alpha}{J} & -\frac{\epsilon v\cos\alpha}{J} & -\frac{\tau_n}{J} \end{pmatrix}, \tag{A4}$$

evaluated at the solution of interest, $(v_0 = \cos(\arctan t_0), \alpha_0 = \arctan t_0, \omega_0 = t_0/\tau_v)$, and, when they exist, $(v_\pm = \cos(\arctan t_\pm), \alpha_\pm = \arctan t_\pm, \omega_\pm = t_\pm/\tau_v)$. For $\epsilon > 0$, all eigenvalues have negative real parts and the solution $(v_0, \alpha_0, \omega_0)$ is linearly stable in all the parameter space. For $\epsilon < 0$, the solution $(v_0, \alpha_0, \omega_0)$ is stable, respectively, unstable, for $\tau_v/\tau_n < 1$, respectively, $\tau_v/\tau_n > 1$, irrespectively of the values of J.

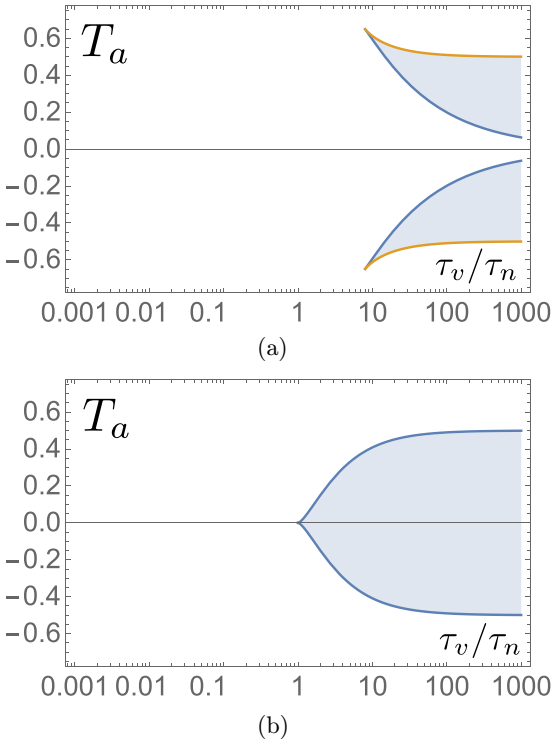

FIG. 10. Domains of existence of real fixed points: The polynomial equation (A3) always has at least one real solution and three real solutions in the shaded domains: (a) aligners, $\epsilon = +1$; (b), fronters, $\epsilon = -1$.

b. Case $T_a \neq 0$

Let us set $T_a > 0$, the case $T_a < 0$, being perfectly symmetric. The coefficients of the third-order polynomial (A3) being real, the number of real solutions is given by the sign of its discriminant Δ: there are three, respectively, one, real solution, when $\Delta > 0$, respectively, $\Delta < 0$. In the present case, $\Delta = 4T_a^4 + (8a^2 - 20a\epsilon - 1)T_a^2 + (4a\epsilon^3 + 12a^2 + 12a^3\epsilon + 4a^4)$, with $a = \tau_n/\tau_v$. The regions with $\Delta > 0$ are shaded in gray in Fig. 10 for, respectively, the aligner and the fronter case. The corresponding families of solutions are obtained semianalytically and are shown, respectively, in Figs. 3 and 4.

The linear stability analysis follows the same path as above, with the same Jacobian, because the active torque is a simple constant. In the present case, one must evaluate the sign of the real part of the eigenvalues numerically around the solutions found above. In the case $\epsilon = +1$, the stability scheme is rather simple. The solution that deforms continuously from the unique linearly stable solution obtained when $T_a = 0$ remains stable. As expected for a saddle node bifurcation, one of the bifurcated solution is stable, here the one with the largest α, and the other is linearly unstable. These results are independent of the value of J. In the case $\epsilon = -1$, the numerical analysis leads to a less trivial dependance on J summarized in Fig. 5.

2. Dynamics along the wall

We start with Eqs. (8) of the main text:

$$\tau_v \ddot{x} = \cos\theta - \dot{x} - \kappa N_w(x), \tag{A5a}$$

$$\tau_v \ddot{y} = \sin\theta - \dot{y} - v(\dot{y} + \dot{\theta}/2), \tag{A5b}$$

$$J\ddot{\theta} = \epsilon(\cos\theta\,\dot{y} - \sin\theta\,\dot{x}) - \tau_n\dot{\theta} - \tau_r(\dot{y} + \dot{\theta}/2). \tag{A5c}$$

The dynamics reduced to the motion along the wall can be rewritten as four first-order differential equations for the variables $(y, z = \dot{y}, \theta, \omega = \dot{\theta})$,

$$\dot{y} = z, \tag{A6a}$$

$$\tau_v \dot{z} = \sin\theta - (1 + v)z - v\omega/2, \tag{A6b}$$

$$\dot{\theta} = \omega, \tag{A6c}$$

$$J\dot{\omega} = (\epsilon\cos\theta - \tau_r)z - (\tau_r/2 + \tau_n)\omega, \tag{A6d}$$

from which one finds the trivial fixed points $(y = 0, z = 0, \theta = 0, \omega = 0)$ and $(y = 0, z = 0, \theta = \pi, \omega = 0)$. The first one is the only relevant one, since the second one would describe a particle going away from the wall, and therefore escape the description of the dynamics reduced to the direction along the wall. The Jacobian of the dynamics evaluated at the fixed point $(y = 0, z = 0, \theta = 0, \omega = 0)$ reads

$$K = \begin{pmatrix} 0 & 1 & 0 & 0 \\ 0 & -\frac{1+v}{\tau_v} & \frac{1}{\tau_v} & -\frac{v}{2\tau_v} \\ 0 & 0 & 0 & 1 \\ 0 & \frac{\epsilon - \tau_r}{J} & 0 & -\frac{\frac{\tau_r}{2} + \tau_n}{J} \end{pmatrix}, \tag{A7}$$

where one immediately sees that there is a zero eigenvalue associated with the marginal stability of the fixed point, for all values of the parameters, that corresponds to the translational invariance of the dynamics along the wall. In the absence of a simple analytical expression for the eigenvalues, one has to rely on a careful, but straightforward, parametric analysis of the above Jacobian to derive the main features summarized in the main text.

[1] S. Ramaswamy, Annu. Rev. Condens. Matter Phys. **1**, 323 (2010).
[2] T. Vicsek and A. Zafeiris, Phys. Rep. **517**, 71 (2012).
[3] M. C. Marchetti, J.-F. Joanny, S. Ramaswamy, T. B. Liverpool, J. Prost, M. Rao, and R. A. Simha, Rev. Mod. Phys. **85**, 1143 (2013).
[4] C. Bechinger, R. Di Leonardo, H. Löwen, C. Reichhardt, G. Volpe, and G. Volpe, Rev. Mod. Phys. **88**, 045006 (2016).
[5] X. L. Wu and A. Libchaber, Phys. Rev. Lett. **84**, 3017 (2000).
[6] C. Dombrowski, L. Cisneros, S. Chatkaew, R. E. Goldstein, and J. O. Kessler, Phys. Rev. Lett. **93**, 098103 (2004).
[7] H. P. Zhang, A. Be'er, E. L. Florin, and H. L. Swinney, Proc. Natl. Acad. Sci. USA **107**, 13626 (2010).
[8] F. Peruani, J. Starruß, V. Jakovljevic, L. Søgaard-Andersen, A. Deutsch, and M. Bär, Phys. Rev. Lett. **108**, 098102 (2012).
[9] B. Szabó, G. Szöllösi, B. Gönci, Z. Jurányi, D. Selmeczi, and T. Vicsek, Phys. Rev. E **74**, 061908 (2006).
[10] B. Smeets, R. Alert, J. Pesek, I. Pagonabarraga, H. Ramon, and R. Vincent, Proc. Natl. Acad. Sci. USA **113**, 14621 (2016).

[11] G. Peyret, R. Mueller, J. d'Alessandro, S. Begnaud, P. Marcq, R.-M. Mège, J. M. Yeomans, A. Doostmohammadi, and B. Ladoux, Biophys. J. **117**, 464 (2019).
[12] A. Walther and A. H. E. Müller, Soft Matter **4**, 663 (2008).
[13] J. Palacci, C. Cottin-Bizonne, C. Ybert, and L. Bocquet, Phys. Rev. Lett. **105**, 088304 (2010).
[14] J. Palacci, S. Sacanna, A. P. Steinberg, D. J. Pine, and P. Chaikin, Science **339**, 936 (2013).
[15] X. Zheng, B. Ten Hagen, A. Kaiser, M. Wu, H. Cui, Z. Silber-Li, and H. Löwen, Phys. Rev. E **88**, 032304 (2013).
[16] I. Buttinoni, J. Bialké, F. Kümmel, H. Löwen, C. Bechinger, and T. Speck, Phys. Rev. Lett. **110**, 238301 (2013).
[17] F. Ginot, I. Theurkauff, D. Levis, C. Ybert, L. Bocquet, L. Berthier, and C. Cottin-Bizonne, Phys. Rev. X **5**, 011004 (2015).
[18] A. Bricard, J.-B. Caussin, N. Desreumaux, O. Dauchot, and D. Bartolo, Nature (London) **503**, 95 (2013).
[19] D. Geyer, A. Morin, and D. Bartolo, Nat. Mater. **17**, 789 (2018).
[20] A. Cavagna and I. Giardina, Annu. Rev. Condens. Matter Phys. **5**, 183 (2014).
[21] A. Attanasi, A. Cavagna, L. Del Castello, I. Giardina, T. S. Grigera, A. Jelić, S. Melillo, L. Parisi, O. Pohl, E. Shen *et al.*, Nat. Phys. **10**, 691 (2014).
[22] A. Kudrolli, G. Lumay, D. Volfson, and L. S. Tsimring, Phys. Rev. Lett. **100**, 058001 (2008).
[23] J. Deseigne, O. Dauchot, and H. Chaté, Phys. Rev. Lett. **105**, 098001 (2010).
[24] C. A. Weber, T. Hanke, J. Deseigne, S. Léonard, O. Dauchot, E. Frey, and H. Chaté, Phys. Rev. Lett. **110**, 208001 (2013).
[25] N. Kumar, H. Soni, S. Ramaswamy, and A. K. Sood, Nat. Commun. **5**, 4688 (2014).
[26] L. Giomi, N. Hawley-Weld, and L. Mahadevan, Proc. R. Soc. A **469**, 20120637 (2013).
[27] E. Ferrante, A. E. Turgut, C. Huepe, A. Stranieri, C. Pinciroli, and M. Dorigo, Adapt. Behav. **20**, 460 (2012).
[28] M. Rubenstein, A. Cornejo, and R. Nagpal, Science **345**, 795 (2014).
[29] M. Y. Ben Zion, J. Fersula, N. Bredeche, and O. Dauchot, Sci. Rob. **8**, eabo6140 (2023).
[30] C. Scholz, S. Jahanshahi, A. Ldov, and H. Löwen, Nat. Commun. **9**, 5156 (2018).
[31] H. Löwen, J. Chem. Phys. **152**, 040901 (2020).
[32] A. R. Sprenger, L. Caprini, H. Löwen, and R. Wittmann, J. Phys.: Condens. Matter **35**, 305101 (2023).
[33] P. Baconnier, O. Dauchot, V. Démery, G. Düring, S. Henkes, C. Huepe, and A. Shee, arXiv:2403.10151.
[34] N. Shimoyama, K. Sugawara, T. Mizuguchi, Y. Hayakawa, and M. Sano, Phys. Rev. Lett. **76**, 3870 (1996).
[35] S. Henkes, Y. Fily, and M. C. Marchetti, Phys. Rev. E **84**, 040301(R) (2011).
[36] K.-D. Nguyen Thu Lam, M. Schindler, and O. Dauchot, New J. Phys. **17**, 113056 (2015).
[37] C. Malinverno, S. Corallino, F. Giavazzi, M. Bergert, Q. Li, M. Leoni, A. Disanza, E. Frittoli, A. Oldani, E. Martini *et al.*, Nat. Mater. **16**, 587 (2017).
[38] D. L. Barton, S. Henkes, C. J. Weijer, and R. Sknepnek, PLoS Comput. Biol. **13**, e1005569 (2017).
[39] F. Giavazzi, M. Paoluzzi, M. Macchi, D. Bi, G. Scita, M. L. Manning, R. Cerbino, and M. C. Marchetti, Soft Matter **14**, 3471 (2018).
[40] V. Petrolli, M. Le Goff, M. Tadrous, K. Martens, C. Allier, O. Mandula, L. Hervé, S. Henkes, R. Sknepnek, T. Boudou *et al.*, Phys. Rev. Lett. **122**, 168101 (2019).
[41] P. Baconnier, D. Shohat, C. H. López, C. Coulais, V. Démery, G. Düring, and O. Dauchot, Nat. Phys. **18**, 1234 (2022).
[42] P. Baconnier, D. Shohat, and O. Dauchot, Phys. Rev. Lett. **130**, 028201 (2023).
[43] See Supplemental Material at http://link.aps.org/supplemental/10.1103/PhysRevE.110.014606 for further visual evidences of our main observations with 4 videos.
[44] O. Dauchot and V. Démery, Phys. Rev. Lett. **122**, 068002 (2019).
[45] K.-D. N. T. Lam, M. Schindler, and O. Dauchot, J. Stat. Mech.: Theory Exp. (2015) P10017.
[46] J. Deseigne, S. Léonard, O. Dauchot, and H. Chaté, Soft Matter **8**, 5629 (2012).